Electron Partial Density and Temperature Over Jupiter's Main Auroral Emission Using Juno Observations

F. Allegrini, W. S. Kurth, S. S. Elliott, J. Saur, G. Livadiotis, G. Nicolaou, F. Bagenal, S. Bolton, G. Clark, J. E. P. Connerney, et al.

JGR Space Physics

RESEARCH ARTICLE
10.1029/2021JA029426

Electron Partial Density and Temperature Over Jupiter's Main Auroral Emission Using Juno Observations

F. Allegrini[1,2], W. S. Kurth[3], S. S. Elliott[3], J. Saur[4], G. Livadiotis[1], G. Nicolaou[1], F. Bagenal[5], S. Bolton[1], G. Clark[6], J. E. P. Connerney[7,8], R. W. Ebert[1,2], G. R. Gladstone[1,2], P. Louarn[9], B. H. Mauk[6], D. J. McComas[10], A. H. Sulaiman[3], J. R. Szalay[10], P. W. Valek[1], and R. J. Wilson[5]

[1]Southwest Research Institute, San Antonio, TX, USA, [2]Department of Physics and Astronomy, University of Texas at San Antonio, San Antonio, TX, USA, [3]Department of Physics and Astronomy, University of Iowa, Iowa City, IA, USA, [4]Institute of Geophysics and Meteorology, University of Cologne, Cologne, Germany, [5]Laboratory for Atmospheric and Space Physics, University of Colorado Boulder, Boulder, CO, USA, [6]The Johns Hopkins University Applied Physics Laboratory, Laurel, MD, USA, [7]Space Research Corporation, Annapolis, MD, USA, [8]NASA Goddard Space Flight Center, Greenbelt, MD, USA, [9]Institut de Recherche en Astrophysique et Planétologie (IRAP), Toulouse, France, [10]Department of Astrophysical Sciences, Princeton University, Princeton, NJ, USA

Key Points:

- We present a survey of auroral electrons properties (partial density and temperature) over Jupiter's main auroral region
- The electron density (temperature) increases (decreases) equatorward of the main oval, and density and temperature are anti-correlated
- The ratio of B/n follows the same trend as the electron characteristic energy and is maximum near the main oval

Supporting Information:

Supporting Information may be found in the online version of this article.

Correspondence to:

F. Allegrini,
fallegrini@swri.edu

Citation:

Allegrini, F., Kurth, W. S., Elliott, S. S., Saur, J., Livadiotis, G., Nicolaou, G., et al. (2021). Electron partial density and temperature over Jupiter's main auroral emission using Juno observations. *Journal of Geophysical Research: Space Physics*, *126*, e2021JA029426. https://doi.org/10.1029/2021JA029426

Received 9 APR 2021
Accepted 17 AUG 2021

Abstract We present a survey of electron partial densities (i.e., the portion of the total density measured between ~0.05 and 100 keV) and temperatures in Jupiter's main auroral emission region using plasma measurements from the Jovian Auroral Distributions Experiment (JADE) on Juno. The electron partial density increases from ~0.01 or 0.1 cm^{-3} near the main oval to a few cm^{-3} at the edge of the measurable part of the UV emission equatorward of the main oval. The electron temperature is highest near the main oval at ~10–20 keV and decreases equatorward down to ~0.3–2 keV. The JADE electron partial density agrees within a factor of ~2 with the total electron densities derived from Juno-Waves when the comparison is possible. The electron density and temperature trends are consistent for all sampled longitudes, for the north and the south, and there is no significant trend with radial distance in the range examined in this study (1.25–1.96 R_J). The electron density is anti-correlated with the temperature and the characteristic energy. The ratio of the magnetic field strength to the electron density is maximum near the main oval.

Plain Language Summary The very intense ultraviolet (UV) aurora at Jupiter is caused by energetic electrons precipitating from the magnetosphere into the atmosphere where they excite molecular hydrogen. The Jovian Auroral Distributions Experiment (JADE) on Juno measures electron pitch angle and energy distributions from ~50 eV to ~100 keV. Investigating the characteristics of electron distributions at these energies is critical for understanding the source population for the electrons that produce Jupiter's UV aurora and the mechanisms that accelerate them to keV and MeV energies. In this study, we present a survey of electron densities and temperatures derived from JADE in Jupiter's polar magnetosphere. The electron density from JADE agrees very well with that obtained from Juno's Waves instrument, using a different and independent method. We find that the electron densities over the main emissions increase with decreasing latitudes and the electron temperatures increase with increasing latitudes. These trends are independent of longitude, hemisphere, or altitude. The electron density and temperature are anti-correlated. The ratio of the magnetic field strength to the electron density is maximum near the main oval where accelerated electron distributions are observed.

1. Introduction

Major progress has been made in our understanding of the Jovian magnetosphere in the last few decades. The Jupiter system—planet, moons, and magnetosphere—has been visited a number of times by various missions, either flying by (Pioneer, Voyager, Ulysses, Cassini, and New Horizons) or orbiting Jupiter (Galileo, Juno). Each of those missions contributed in situ observations that complement the more global and remote observations (e.g., radio, UV) taken from Earth or Earth's orbit.

We know that the dynamics of the Jovian magnetosphere are dominated and mostly powered by the fast rotation of the planet and its strong magnetic field (reviewed by Bagenal et al., 2017; Krupp et al., 2004;

McComas & Bagenal, 2007). The moon Io injects roughly a ton per second of volcanic material (S and O) into Jupiter's magnetosphere. This creates a plasma torus in the vicinity of Io's orbit (reviewed by Bagenal & Dols, 2020; Thomas et al., 2004) and a plasma disk extending radially outward that is, almost rigidly co-rotating with the planet out to about 20–30 Jovian radii or R_J (1 R_J = 71,492 km). The plasma disk is confined to the equator due to strong centrifugal forces. To enforce this rotation, momentum is transferred from the planet to the plasma disk through a current system that couples the equatorial magnetosphere to the high-latitude polar magnetosphere with closure in the ionosphere (Cowley & Bunce, 2001; Khurana et al., 2004; Hill 1979, 2001). Electrons and ions are accelerated and precipitate into the atmosphere to create the most intense aurora in the solar system (e.g., Clarke et al., 1998, 2004).

Until the arrival of Juno at Jupiter in 2016, in situ observations of the plasma were made mostly in the equatorial region, close to the plasma sheet and down the magnetospheric tail (McComas et al., 2007). Using the Voyager Plasma Science Experiment (PLS), Scudder et al. (1981) surveyed electron populations (10 eV–5.95 keV) as close as 5.5 R_J. Typical electron densities in the outer magnetosphere (~33–46 R_J) were about 10^{-3} to 10^{-2} cm^{-3}, with temperatures in the 2–3 keV range. The electron distributions showed multiple populations with a Maxwellian cold population and suprathermal tails at the higher energies. Closer in (5.5–13 R_J), the electron populations were predominantly Maxwellian, with electron densities ranging from ~10 cm^{-3} to a few 10^3 cm^{-3}; temperatures decrease with decreasing radial distance from ~100 eV, dropping down to less than ~2 eV at ~5 R_J (Sittler & Strobel, 1987).

After re-analysis of Voyager 1 and 2 plasma wave (PWS) data, Barnhart et al. (2009) determined that the electron densities are around 10^{-1} to 10^0 cm^{-3} at ~20 R_J, falling to ~10^{-2} cm^{-3} by ~50 R_J, with large variations of more than one order of magnitude.

Bagenal et al. (2016) reported plasma observations from Galileo PLS. They found that the plasma density near the centrifugal equatorial plane decreases from about 2,000 cm^{-3} in the Io plasma torus down to about 0.05 cm^{-3} at 30 R_J. As for the ion temperature, it increases with radial distance from about 60-80 eV at ~6 R_J up to a few keV at 30 R_J. There is no persistent or systematic variation of neither density nor temperature with longitude or local time. An energetic particle population with separate and distinct characteristics (Mauk et al., 2004) coexists with the cold and warm plasma population.

Bame et al. (1992) reported Ulysses electron observations during the flyby that sent the spacecraft into a highly inclined orbit around the Sun. The densities inside the magnetosphere within about 80 R_J ranged from a few 10^{-3} to 10^{-1} cm^{-3} (depending on where Ulysses was with respect to the plasma sheet), and the temperature was around 120–170 eV. While the outbound trajectory left the equatorial plane, the instrument was turned back on only at a distance of 13.9 R_J, and no close-in, high-latitude electron measurements were taken.

Juno's orbits allow sampling of the magnetosphere at high latitudes in the auroral regions near an altitude around 1 R_J or less above the 1-bar level (Bolton et al., 2017). These observations provide new information to help us understand the acceleration processes in the auroral regions and possibly constrain models. For example, the Knight relationship (Knight, 1973) used by Cowley and Bunce (2001) depends on the electron number density and temperature. Similarly, the dissipation at the electron inertial length scale (e.g., Damiano et al., 2019; Saur et al., 2018) also depends on the electron density and temperature.

In this study, we determine the partial electron density and temperature from numerical moments using electron measurements from the Jovian Auroral Distributions Experiment (JADE; McComas et al., 2017) on Juno. We use the phrase “partial density” because some of the electron distribution that contributes to the total electron density falls outside JADE's energy range and cannot be taken into account. However, if most of the distribution falls within JADE's energy range, then the partial density approaches the total electron density. We use the first eight science perijove passes (PJ 1, 3, 4... 9), north and south, for which the spacecraft orientation along the orbit is favorable to obtain adequate electron pitch angle coverage.

In the next section, we begin by presenting the overview of a case study (PJ9 south). We then focus on the details of the partial electron density and temperature observations. We compare the derived partial electron density with the total electron density derived from the Waves experiment on Juno (Kurth et al., 2017). We present similar observations for all eight perijoves. Then, we examine the relationships between the

partial electron density, the temperature, and the characteristic electron energy, and we show that these quantities are correlated in the auroral regions. We also show that the ratio of the magnetic field strength to the electron density increases with magnetic latitude. Finally, we conclude with a summary of our findings.

2. Observations

2.1. Overview of Perijove 9 South

Figure 1 provides the context and an overview of the electron data during Juno's science perijove 9 in the south. Panel (a) shows Juno's magnetic footprint track on a reconstructed UltraViolet Spectrometer (UVS, Gladstone et al., 2017) image in false color. Panel (b) shows a projection of Juno's trajectory in a magnetic reference frame (JRM09+CAN1981, see below). Jupiter's current sheet stretches the field lines near the equator, resulting in a significant difference with respect to a simple dipolar magnetic field configuration. In order to reflect this difference, we use the terminology M-shell instead of the magnetic dipole *L*-shell (McIlwain, 1961). We derive the M-shell distance using the latest magnetic field model JRM09 (Connerney et al., 2018) and a current sheet model (Connerney et al., 1981, 1998), hereafter abbreviated as JRM09+CAN1981.

The thick part of the track in Panels (a and b) corresponds to the time of panels (c) through (e). Panel (c) shows an electron intensity spectrogram, and panel (e) shows the pitch angle distribution (0°/180° correspond to electrons moving toward/away from Jupiter for this southern perijove pass) for energies between 50 eV and 100 keV. Panel (d) shows the total energy flux in blue for upward (pitch angles from 0 to 31.6°) and in red for downward (pitch angles from 148.4° to 180°) electrons for energies between 50 eV and 1 MeV. Most of the electron observations reported here were made by the JADE (McComas et al., 2017). However, the total energy flux also includes data from the Juno Energetic particle Detector Instrument (JEDI, Mauk, Haggerty, Jaskulek, et al., 2017) and was reported in Allegrini, Mauk, et al. (2020).

The JADE electron sensors (JADE-E) consist of two identical spherical top-hat electrostatic analyzers with external deflectors and microchannel plate detectors. JADE-E uses an on-board, broadcast magnetic field vector to determine the deflection angle and measure the magnetic field-aligned electrons. In the auroral region, JADE-E measures the energy and pitch angle distributions of electrons at its highest time resolution of 1s. Here, we use the calibrated, level 3 version 3 data at NASA's Planetary Data System (PDS) (which is available at the site identified in the Acknowledgments section). That data contain a background estimate based on a separate background measurement (see Text S2), and it is already subtracted from the signal. The conversion from counts per second to intensities uses updated sensitivity factors described in Text S1. We calculate the pitch angle using the local magnetic field provided by the MAG experiment (Connerney et al., 2017).

For this interval, the jovigraphic latitude of Juno ranges from −62.2° to −77.5°, the M-shell from ∼5.7 to ∼62, the jovigraphic distance from 1.63 to 2.06 R_J, and the magnetic field strength from 1.67 to 0.92 Gauss.

To position the electron observations with respect to the UV observations and to previous work, we use the zones defined in Mauk et al. (2020). They defined zones in the auroral region based on recurring characteristics of the high energy electron populations. In summary, these zones are:

1. DifA–Diffuse Aurora: (a) The intensities outside the loss cone are larger than inside the loss cone and (b) the intensities and energy fluxes within the loss cone are greater downward than upward.
2. ZI(D) – Zone I Downward: (a) The intensities inside the downward loss cone are greater than outside the downward loss cone and (b) the intensities and energy fluxes downward are greater than upward.
3. ZII(B) – Zone II Bidirectional: (a) The intensities inside the upward loss cone are greater than outside the upward loss cone, (b) the upward intensities and energy fluxes are greater than the downward intensities and energy fluxes, and (c) the downward fluxes are sufficient to stimulate powerful auroral emissions
4. Polar Cap–it is characterized by two main features: (a) Broadband electron beams streaming out of at least portions of the polar caps are persistent upward and narrowly collimated (Mauk, Haggerty, Paranicas, et al., 2017) and (b) large-scale, downward, magnetic field-aligned electrostatic potentials often exceeding megavolt levels are observed for ∼80% of the time (Clark et al., 2017)

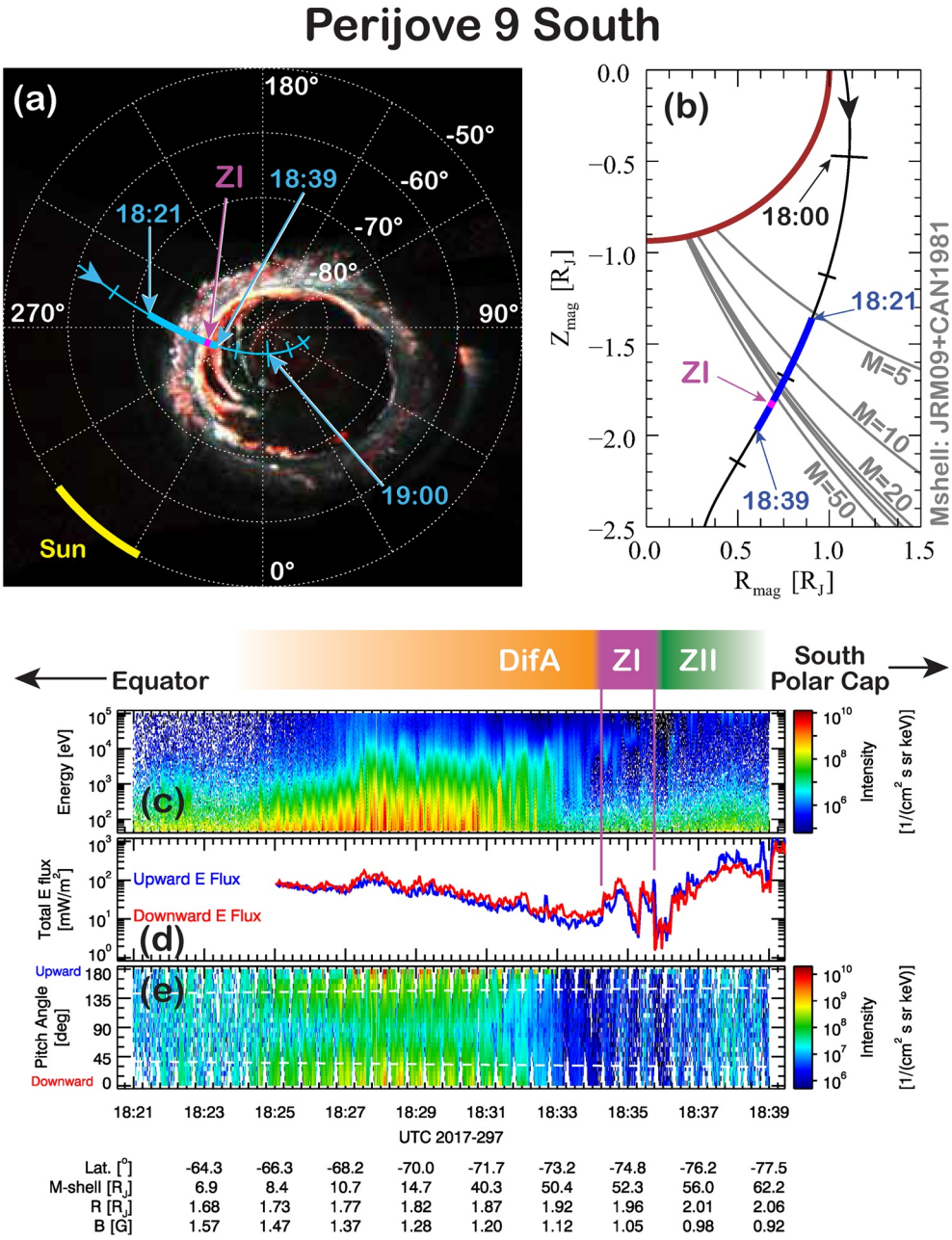

Figure 1. (a) UV false color image with Juno's magnetic footprint track for perijove 9 south. (b) Juno trajectory in a magnetic coordinate system. The *M*-shell mapping is according to JRM09+CAN1981. The thicker parts of the track in (a and b) correspond to the time interval of panels (c–e). Electron intensities are shown as a function of (c) energy and (e) pitch angle for 50 eV–100 keV, and total energy flux (d) for 50 eV–1 MeV electrons. The zones defined in Mauk et al. (2020) are shown on top of panel (c), with ZI between ~18:34:15 and ~18:35:45 (see text for more details).

We indicate the three zones DifA, ZI, and ZII on top of panel (c) with colored bars. The transition between the DifA and ZI zones occurs at ~18:34:15, and from ZI to ZII at ~18:35:45. ZI coincides with the double peak in the total energy flux (panel d). ZI also correspond to the most intense upward electric currents as determined from perturbations in the magnetic field by Kotsiaros et al. (2019). Equatorward of this double peak in the energy flux, there is a region where the lower-than ~30 keV electrons usually dominate the contributions to the total energy flux (from ~18:30:15 to 18:34:30; Allegrini, Mauk, et al., 2020). This particular pass shows some intense emissions in ZII (after ~18:35:45) that add structure and complexity to the observations.

2.2. Density and Temperature

Figure 2a shows the electron differential energy flux from 50 eV to 100 keV as a function of time. Using the background estimate (Text S2), we calculate the signal-to-noise ratio (SNR) in panel (b) as a function of time and energy. Panel (c) shows the signal (green) and the background (gray) in counts/s averaged over all look directions and energies, and the SNR (black) as a function of time. Panels (d and e) show the partial electron density (50 eV–100 keV) and the electron temperature, both derived from numerical integration. We use Equations 6.1 to 6.10 in Section 6.2.1 of Paschmann and Daly (1998). The count rates from JADE-E's look directions were re-binned in pitch angle space with 15° bins. We describe the JADE data selection to derive the partial density and temperature further below. The dark blue "+" symbols are at 1-s time resolution of the JADE instrument, and the lighter blue curves are 30-s averages. Panel (d) also shows the total electron density derived by Waves in violet and dark red (from Elliott et al., 2021).

Because plasma waves have characteristic frequencies dependent on the electron density, plasma wave instruments have various ways of obtaining electron densities. The measurements from Waves presented in this study use two spectral features for density determination: the lower cutoff of ordinary mode emissions at the local electron plasma frequency and the frequency of detected plasma oscillations at the local electron plasma frequency. The electron plasma frequency is a simple function of the electron density $f_{pe} = 8{,}980^{*}(n_e)^{1/2}$. Strictly speaking, the low-frequency cutoff of ordinary mode emissions is an upper limit of the plasma frequency, since it is possible that a higher-density region between the wave source and the observer can be responsible for the cutoff. More detail on these two methods can be found in Elliott et al. (2021). The dark red symbols correspond to the method that uses the low-frequency cutoff of ordinary mode emissions, and the violet symbols correspond to the method that uses the frequency of plasma oscillations at the local electron plasma frequency.

We use three criteria to select the JADE data for determination of the partial density and temperature: (a) the signal-to-noise ratio (SNR) is above 2, (b) the pitch angle coverage is full, and (c) the peak contribution of the partial density per energy channel is within JADE's energy range.

The SNR (Figure 2c) threshold is a straightforward criterion. Nevertheless, a little more details on the SNR are relevant at this point. The electron sensors in JADE use microchannel plate detectors to count the electrons that passed through the electrostatic analyzer (ESA). This method of counting is also sensitive to events from penetrating radiation (e.g., >5–10 MeV electrons) that can also create counts on top of the signal. A count from penetrating radiation is indistinguishable from a legitimate electron count in the front-end electronics. However, JADE is equipped with a background measuring anode inaccessible to legitimate electrons traveling inside the ESA. Therefore, we independently estimate the background at any time and subtract it from the signal. In this paper, we set a SNR (or signal-to-background ratio) threshold of 2 as a criterion for determination of the density and the temperature.

While a threshold of 2 may seem low, it is better than it looks. The SNR used as a criterion (Figure 2c) is averaged over energies and look directions. However, looking at Figure 2a or 2b, one sees that the flux (or signal) is not spread uniformly over the energy range. For example, between 18:28:15 and 18:28:30, the maximum SNR from panel (b) is ∼2–∼5 times greater than the average SNR from panel (c). Therefore, when calculating the numerical moments, the largest contributions to the partial densities and temperatures come from a significantly higher SNR than the average SNR of 2 (our threshold in this study). And finally, note that increasing the threshold to higher values (e.g., 5), does not appreciably change the results that follow, nor does it modify the main conclusions of this study; but it does reduce the number of data points that we can work with.

While a necessary condition, the SNR alone is not sufficient to evaluate whether the measurement is reliable to determine the partial electron density within a reasonable factor of the total electron density. Our second criterion is that the pitch angle coverage should also be as complete as possible in order to account for the whole distribution during the integration. For example, if there were angle beams in the electron distributions that were outside JADE's field-of-view (FOV), then the results of the numerical moments would be missing this important component of the distribution. Our second criterion ensures that this does not happen.

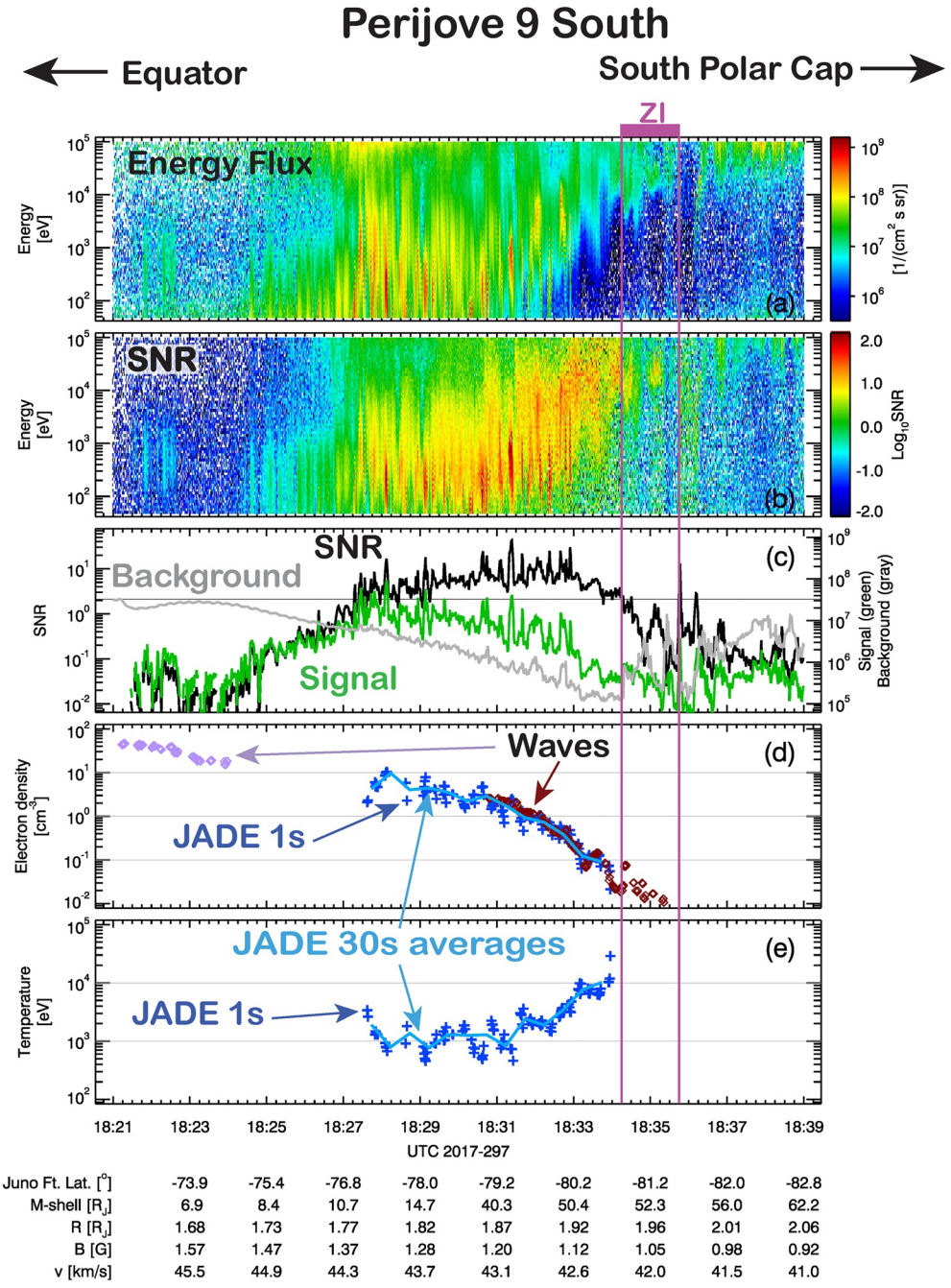

Figure 2. (a) Differential electron energy flux as a function of energy and time. (b) Signal-to-noise ratio (SNR) as a function of energy channel. (c) SNR (black), total background counts per second (gray), and total signal counts per second (green). (d and e) partial electron density (50 eV to 100 keV) and temperature as derived by numerical integration at 1s resolution (blue "+") and 30 s averages (lightblue curve). The violet and dark red symbols in panel (d) show the total electron density derived by Waves (Elliott et al., 2021). There is very good agreement between the partial electron density from Jovian Auroral Distributions Experiment-E and the total electron density from Waves. Juno's footprint latitude (Juno Ft. Lat.), local M-shell, radial distance, local magnetic field strength, and speed are indicated at the bottom of the figure.

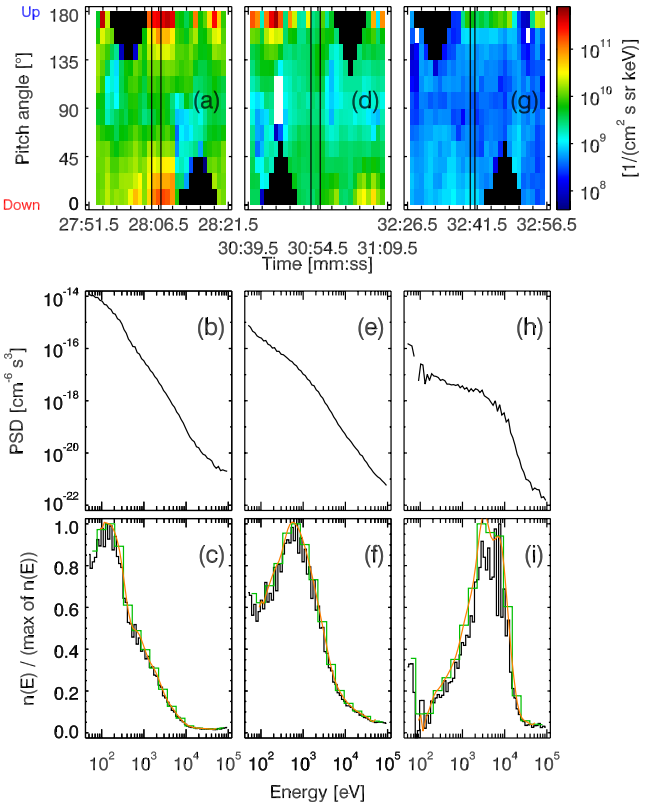

Figure 3. Top row (a, d, and g): electron pitch angle spectrograms for three time intervals. Middle row (b, e, and h): the corresponding phase-space densities. Bottom row (c, f, and i): the black histogram is the partial electron density per energy channel normalized to a maximum of 1, the green histogram is the same with energy channel bins binned by 4, and the orange curve is a spline approximation of the green histogram. The bottom row illustrates which part of the distribution contributes to the partial electron density measured by Jovian Auroral Distributions Experiment (JADE). JADE measures most of the distribution for the third interval (g–i). For the first two intervals (a–f), a fraction of the electron distribution is unaccounted for in the density calculation due to the lower energy cut-off of JADE (50 eV). Therefore, we expect the partial electron density from JADE to be lower than the total electron density.

Table 1
Comparison of the Jovian Auroral Distributions Experiment (JADE) Partial Electron Density With the Waves Total Electron Density for Two Intervals of Figure 3

	Date 2017-297 and time	JADE partial electron density n_{JADE} [cm^{-3}]	Waves total electron density n_{Waves} [cm^{-3}]
Interval 2 Figures 3d–3f	18:30:54 to 18:30:55	1.9	2.5
Interval 3 Figures 3g–3i	18:32:41	0.54	0.38

In Figure 3, we focus on three short (1 s or 2 s) time intervals and show the electron distributions measured by JADE. The top row (panels a, d, and g) shows pitch angle spectrograms and the selected time intervals between the two vertical lines. All three selected intervals have full pitch angle coverage. The black triangles in the spectrograms illustrate when the pitch angle coverage is partial, that is, when JADE-E's field-of-view does not sample that part of the pitch angle distribution. The times of partial pitch angle coverage are not selected for this study.

The middle row of Figure 3 (panels b, e, and h) shows the phase-space densities for each interval. The bottom row of Figure 3 (panels c, f, and i) shows the electron partial density per energy channel normalized to a maximum of 1. The bottom panels are useful to see what part of the distribution contributes to the electron density derived by JADE. For example, panel (i) shows that JADE measured most of the distribution that contributes to the total electron density, and we should expect the partial electron density from JADE to be close to the total electron density. Panel (f) shows that the low-energy cut off does not cover a low energy tail that would contribute to the electron density, and we should expect the JADE partial electron density to be slightly lower than the total electron density. Lastly, panel (c) hints at an even higher portion of the distribution that is unaccounted for at the low energies. Waves can determine the total electron density during the second interval (panels d, e, and f) and the third interval (panels g, h, and i), but not for the first interval (panels a, b, and c). Table 1 shows the measured densities for the last two intervals. As expected, the value from JADE is lower than that from Waves for interval 2. The value from JADE for interval 3 is slightly higher than that from Waves.

That brings us to the third criterion, which is to select times when the peak contribution per energy channel to the density is within JADE's energy range. If the peak contribution is within 200 eV–50 keV (for perijoves 1, 3, 4, 5, and 6; JADE-E's energy range is 100 eV–100 keV) or 100 eV–50 keV (for perijoves 7, 8, and 9; JADE-E's energy range is 50 eV–100 keV), then this criterion is met. When this is the case, then we can argue that most of the contributions to the total density are accounted for. For example, considering the first time interval in Figure 3 (panels a, b, and c), we see that the peak contribution to the density is around 150 eV (panel c). For simplicity, let us assume that the histogram in panel c is symmetrical around the peak. Then, the measured population in JADE's energy range would account for more than half of the total electron density and the contributions of the missing low energy part could only be less than that. Therefore, the error on the density could not exceed a factor of two. However, if there were multiple electron populations contributing outside JADE's energy range (which we would not know about), this criterion would not be adequate.

A way to correct for the missing contributions from the low-energy electrons in panel 3c (and for similar distributions) is to use forward modeling and fit distributions in JADE's energy range. This is a tedious task that needs to be performed at the 1-s cadence of the measurement due to the rapidly changing nature of the distributions (e.g., short duration angle beams).

Figure 2d shows that there is very good qualitative agreement between the densities derived from the JADE-E and Waves observations when the

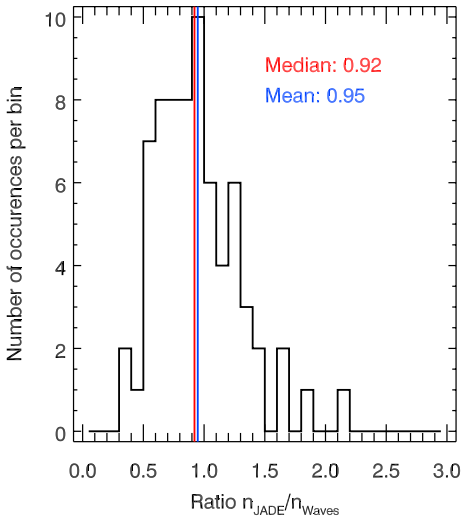

Figure 4. Distribution of the ratio of Jovian Auroral Distributions Experiment partial electron density to Waves total electron density. The mean and the median are indicated in the plot. 94% percent of the occurrences are between 0.5 and 2.

comparison is possible. Similarly, Table 1 shows good agreement for two short intervals. We extend the comparison to all the times when both instruments can derive the electron densities. Figure 4 shows the distribution of the ratio $n_{e,\mathrm{JADE}}/n_{e,\mathrm{Waves}}$, where we used the 30-s averages for JADE and interpolated between the points to match the times from Waves. The average ratio is 0.95 and the median is 0.92. Ninety-four percent of the occurrences fall within a ratio between 0.5 and 2, that is, within a factor of two of each other. Given that Waves accounts for the entire electron population, the number density from JADE-E should be less than or equal to that from Waves, which is supported by the average value lower than 1.

In Figure 5, we show the electron observations from Figure 2 (temperatures in panel (a) and partial densities in panel (c) at 1-s resolution) in the context of the UV emissions in panel (b). The data points, that is, dots, in panels (a and c) are color-coded according to the SNR. The black curves are 20-point averages. The horizontal bars are the footprint latitude range of each 20-point group, and the vertical bars are the standard deviations of each 20-point group. The thin blue lines help connect the electron partial density and temperature with the UV features of the main emission. The violet track in panel (b) corresponds to Io's footprint.

The electron temperature is around ∼1–2 keV when connected to the equatorward part of the main emission from Juno's footprint latitude from approximately −77.5° up to −79° (which corresponds to *M*-shells of ∼12–33 R_J with the model used here). It is similar to the low-latitude Voyager observations in the outer magnetosphere (∼33–46 R_J, Scudder et al., 1981). Moving to higher latitudes, the temperature increases by an order of magnitude until Juno reaches ZI (at latitude ∼81° and M-shell ∼52 R_J). The region where the temperature increases coincides with the region indicated with the double-ended arrow (identified in Allegrini, Mauk, et al., 2020 as where the energy flux of the 3–30 keV precipitating electrons peaks equatorward of the main oval).

Focusing now on Figure 5c, we see that, as Juno's footprint moves poleward starting at about −77°, the partial density decreases from ∼5 cm^{-3} to about 0.1 cm^{-3} or less by the time Juno is connected to ZI. Equatorward of −77° (M-shell of about 11 R_J), JADE cannot determine electron densities. Interestingly, this coincides with where the UV emissions start to dim equatorward. Below about −75°, Waves measures even higher electron densities as Juno gets closer to field lines connected to the Io torus. This suggests that the electron density still increases from ∼ −77° to −75°. Looking at the spectrograms in Figures 1 and 2, we see that the electron energies fall below the lowest energies measured by JADE-E (∼50 eV) equatorward of −77° (before 18:27:20). Therefore, all these observations suggest that the electrons are still present equatorward of about −77°, but the conversion of kinetic energy into UV emission is no longer efficient.

Figure 5 shows that JADE is able to measure electron partial density and temperature when connected to the brighter parts of the UV emissions equatorward of ZI. It is also true for the satellites' footprint tails, which are measured by both UVS and JADE (e.g., Allegrini, Gladstone, et al., 2020; Bonfond et al., 2017; Szalay et al., 2018, 2020), even though Io's footprint tail is not visible because it is too far away in longitude for this pass. Note that Waves makes very good measurements of the electron density in the region connected to the Io torus (Elliott et al., 2021). Poleward of ZI (i.e., ZII and polar cap), the electron energies are usually in the upper end of JADE-E's energy range, or even beyond, and fall within JEDI's energy range (e.g., Clark et al., 2018; Mauk, Haggerty, Paranicas, et al., 2017, 2018; 2020).

The other perijove passes show a similar picture to our case study (PJ9 south) presented above. Figure 6 shows polar projections of the electron partial densities (a and b) and electron temperatures (c and d) from JADE overlaid on reconstructed, false-color UV images (for PJ1 through 9). The images were reconstructed using 40–60 min of UVS data near the main oval crossings and should represent the conditions for each perijove. They are only used qualitatively for context. The electron partial densities peak equatorward of the main emissions, and the electron temperatures peak at the main oval crossings. The minimum and

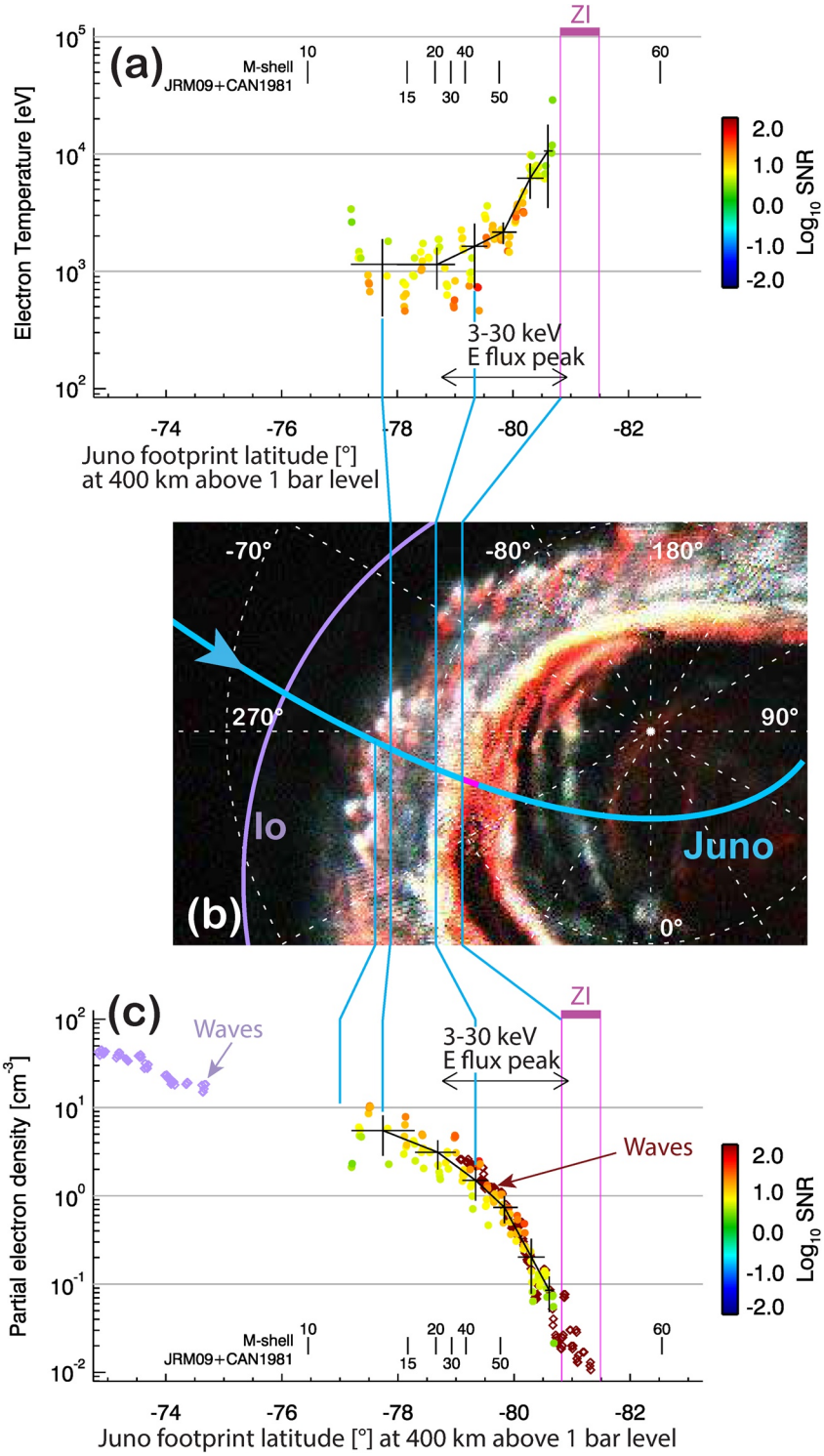

Figure 5. (a) Electron temperature and (c) partial electron density (from Jovian Auroral Distributions Experiment, color-coded dots) and total electron density (from Waves, violet and dark red diamonds) as a function of Juno's magnetic footprint latitude mapped at 400 km above the 1-bar level. (b) False color reconstructed UVS image showing Juno's magnetic footprint and providing context for the electron observations (acquisition time from 18:20:55 to 19:00:55). The purple track is Io's magnetic footprint (JRM09+CAN1981).

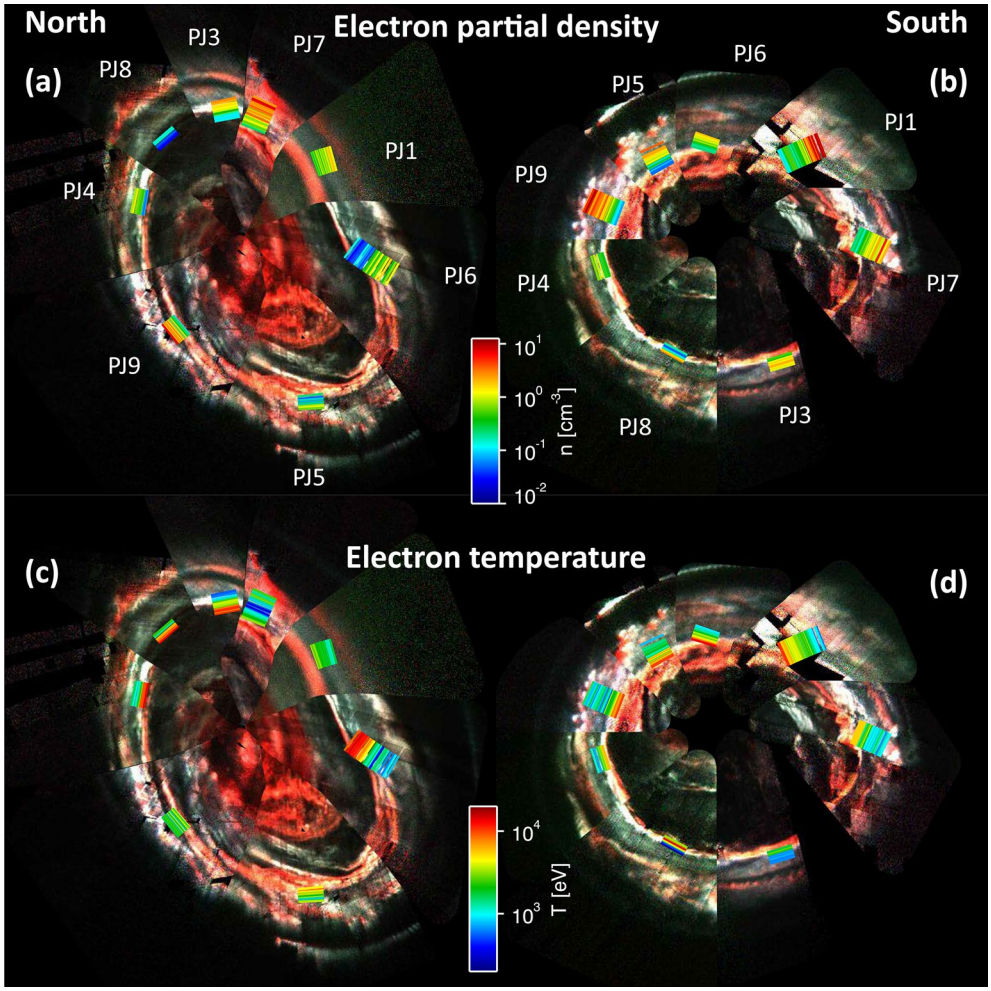

Figure 6. Polar projections of the partial electron density and temperature overlaid with reconstructed, false-color UV images. Top row: partial electron density for (a) the North and (b) the South. Bottom row: electron temperature ((c) North and (d) South). The partial electron density increases equatorward of the main oval. The electron temperature peaks near the main oval.

maximum values of the densities and temperatures are given in Table 2. Note that these first eight orbits were roughly equally distributed in longitude.

Figure 7 shows the same quantities as Figure 6 but in a magnetic reference coordinate system where the abscissa is perpendicular distance from the magnetic axis, and the ordinate is along the JRM09 dipole axis. The same trends are observed, that partial electron density increases with decreasing latitude, and electron temperature increases with increasing latitude. This projection shows that the same pattern exists independent of altitude. We conclude that while there may be small differences from pass to pass, the overall trends depend on M-shell or magnetic latitude and not on (a) System III longitude (Figure 6) or (b) altitude (Figure 7).

2.3. Density, Temperature, and Characteristic Energy

Figure 8 shows the relationships between the electron partial density, n, temperature, T, and characteristic energy, E_{char} (see Equation 1 in Allegrini, Mauk, et al., 2020) for our case study perijove 9 south:

Table 2
Time Intervals When Criteria for Electron Density Determination Are Met and Corresponding Minima and Maxima of the Radial Distance, Electron Partial Density, Electron Temperature, and Exponents of the Fits From Figure 8

PJ	Hemi-sphere	Date YYYY-DDD	Time intervals for electron density determination		Radial distance [R_J]		Electron partial density [cm^{-3}]		Electron temperature [keV]		$T \propto n^{-\alpha}$ $\alpha \pm \sigma_\alpha$	$T \propto E_{Char}^{\alpha}$ $\alpha \pm \sigma_\alpha$	$n \propto E_{Char}^{-\alpha}$ $\alpha \pm \sigma_\alpha$
			Start	Stop	Min	Max	Min	Max	Min	Max			
1	North	2016-240	12:10:10	12:13:17	1.61	1.68	0.46	2.2	0.74	3.3	0.59 ± 0.06	0.30 ± 0.11	0.57 ± 0.2
1	South	2016-240	13:27:36	13:33:03	1.60	1.73	0.11	8.1	0.75	10	0.47 ± 0.03	1.4 ± 0.2	4.2 ± 0.6
3	North	2016-346	16:22:52	16:25:09	1.63	1.69	0.032	2.8	0.75	15	0.79 ± 0.05	1.0 ± 0.1	1.3 ± 0.1
3	South	2016-346	17:35:58	17:37:29	1.50	1.53	0.66	1.7	0.67	2.9	1.1 ± 0.1	0.87 ± 0.20	0.79 ± 0.29
4	North	2017-033	12:24:33	12:26:25	1.46	1.51	0.072	1.00	1.5	12	0.79 ± 0.07	1.2 ± 0.2	1.6 ± 0.2
4	South	2017-033	13:36:30	13:38:40	1.65	1.71	0.23	1.6	1.1	7.2	1.1 ± 0.1	0.78 ± 0.15	0.75 ± 0.08
5	North	2017-086	08:29:29	08:31:17	1.25	1.29	0.11	0.62	1.9	9.1	0.63 ± 0.10	1.8 ± 0.7	3.7 ± 1.2
5	South	2017-086	09:38:03	09:43:43	1.81	1.95	0.052	3.5	0.95	10	0.49 ± 0.18	1.6 ± 0.2	3.3 ± 0.3
6	North	2017-139	05:28:29	05:32:30	1.41	1.49	0.039	0.88	0.67	13	0.87 ± 0.04	1.0 ± 0.1	1.2 ± 0.1
6	South	2017-139	06:49:35	06:52:52	1.86	1.96	0.22	2.3	0.93	11	1.0 ± 0.1	0.95 ± 0.08	0.88 ± 0.12
7	North	2017-192	01:15:55	01:19:14	1.56	1.64	0.18	6.6	0.44	13	0.55 ± 0.11	0.90 ± 0.09	1.6 ± 0.5
7	South	2017-192	02:29:38	02:33:28	1.55	1.64	0.20	3.5	0.83	5.9	0.79 ± 0.06	0.87 ± 0.07	1.1 ± 0.1
8	North	2017-244	21:15:32	21:16:53	1.48	1.52	0.027	0.14	2.6	12	1.0 ± 0.1	1.1 ± 0.2	1.1 ± 0.2
8	South	2017-244	22:26:31	22:28:32	1.61	1.66	0.025	2.2	0.35	18	1.0 ± 0.1	0.93 ± 0.10	0.89 ± 0.12
9	North	2017-297	17:18:54	17:20:50	1.28	1.32	0.073	4.4	1.9	21	0.37 ± 0.06	0.90 ± 0.14	2.5 ± 0.4
9	South	2017-297	18:27:02	18:34:03	1.77	1.94	0.059	7.3	0.74	15	0.59 ± 0.02	1.3 ± 0.1	2.3 ± 0.2

$$E_{char} = \frac{\int_{E_{min}}^{E_{max}} I \cdot E \ dE}{\int_{E_{min}}^{E_{max}} I \ dE} \quad (1)$$

I is the particle intensity (in units of $(cm^2\ s\ sr\ keV)^{-1}$), E is the electron energy (in keV), E_{min} (E_{max}) is the lowest (highest) energy channel from JADE-E. We fit power laws using orthogonal linear regressions in logarithmic space and display the relationships in the plots. The fit parameters are given in Table 2 for all perijove passes used in this study. All the data points from Figure 8 are in the DifA zone, and the vast majority (~98%) of the data points for all perijoves of this study are also in the DifA zone.

Figure 8a shows a negative correlation between the characteristic energy, E_{char}, and the electron partial density, n, that is fitted with a power law ($E_{char} \propto n^{\sim -0.43}$). Assuming that the powering of the aurora is caused by turbulent Alfvénic fluctuations (e.g., Saur et al., 2003, 2018), smaller electron densities lead to larger characteristic energies. The energy is proportional to the inertial electron scale length, λ_e, and the inertial electron scale length is inversely proportional to the square root of the electron density. Thus according to this theory, the energy is inversely proportional to the square root of the electron density. The fit in Figure 8a shows a proportionality factor of 0.43 ± 0.04 in log-log space, close to the expected factor of 0.5.

Figure 8b shows that the electron temperature is roughly proportional to the characteristic energy to the power of ~1.3. Looking at other perijove passes (from PJ1 to PJ9, north and south) we find that this proportionality power-law is ~1.06 on average. The temperature is calculated as the trace of the temperature tensor, $\boldsymbol{T}$, which is derived from the pressure tensor, $\boldsymbol{P}$, using the definition $\boldsymbol{P} \equiv nk\boldsymbol{T}$, where n is the electron density and k is the Boltzmann constant (see Chapter 6 in Paschmann & Daly, 1998). It is often referred to as kinetic temperature. Because the temperature and the thermal energy are related to the thermal velocity with $kT = \frac{1}{2} m v_{th}^2$, we expect proportionality between the temperature and the characteristic energy, that is, $T \propto E_{char}$. Our results show a power index slightly higher than 1 (i.e., ~1.06).

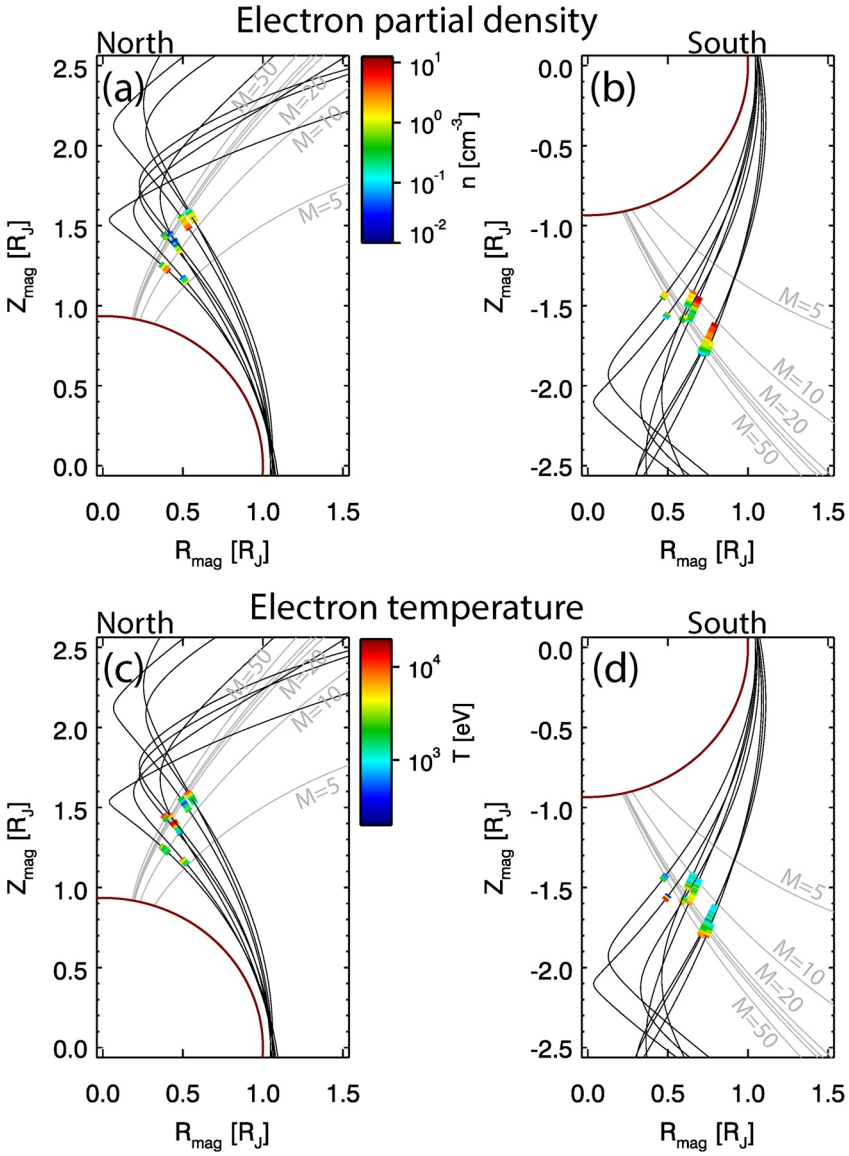

Figure 7. Projection of the electron partial density and temperature in a magnetic reference coordinate system (the abscissa is perpendicular distance from the magnetic axis and the ordinate is along the JRM09 dipole axis). The density increases with decreasing magnetic latitude (or *M*-shell), while the temperature increases with magnetic latitude (or *M*-shell).

Figure 8c shows that the electron temperature is roughly inversely proportional to the square root of the electron partial density, which is consistent with the expected proportionalities between n and E_{char}, and T and E_{char} (explained above).

There is a large scatter in the exponent values in Table 2 (last three columns). This could reflect significant differences in the UV emissions from perijove to perijove as illustrated in Figure 6. We find that on average $T \propto n^{-0.76}$, $T \propto {E_{Char}}^{1.06}$, and $n \propto {E_{Char}}^{-1.74}$.

2.4. Ratio *B*/*N*

A number of arguments show that a parallel electric field (e.g., capable of accelerating electrons above the auroral region) forms where the ratio of the magnetic field strength, B, to the electron density, n, is largest. Lysak and Hudson (1979) show that a parallel electric field can form where the drift velocity for current

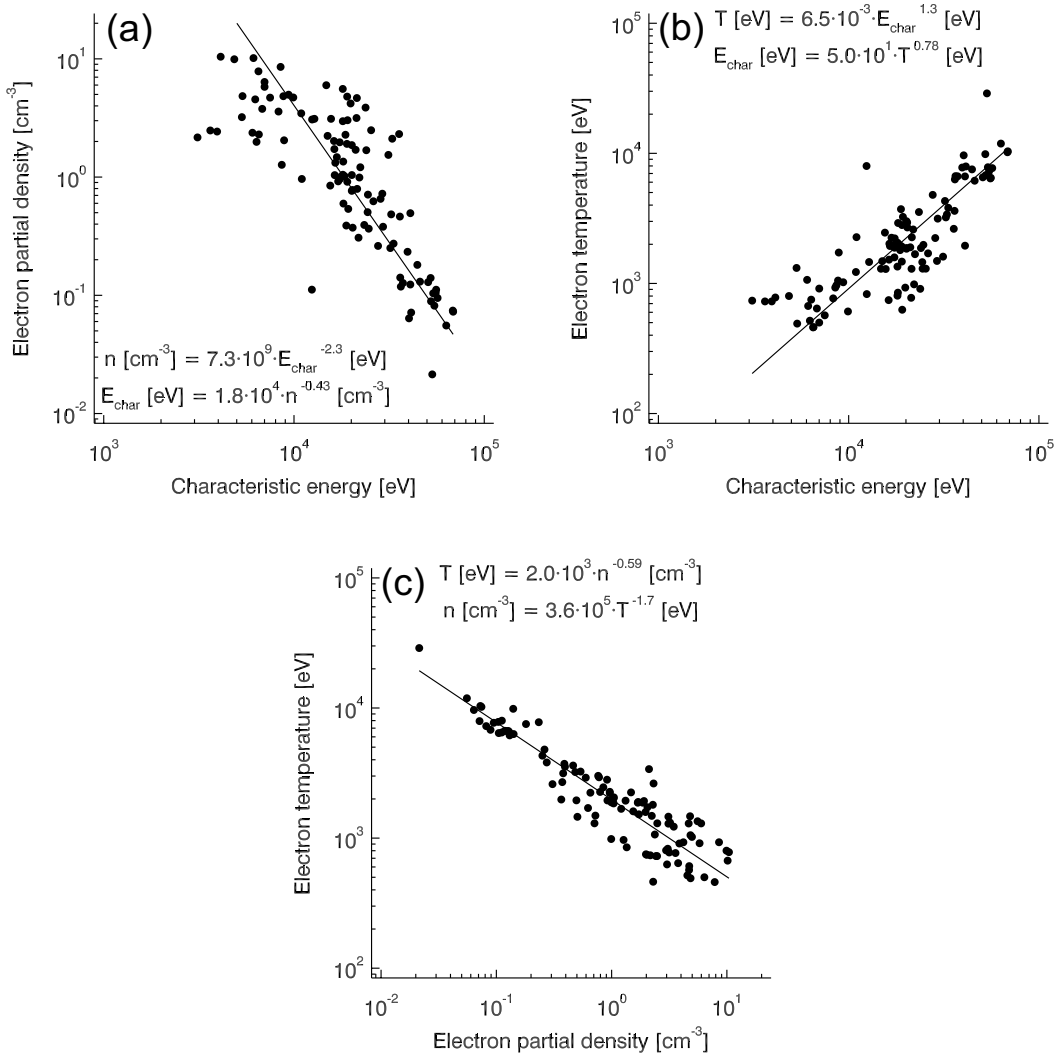

Figure 8. (a) Electron partial density as a function of electron characteristic energy. (b) Electron temperature as a function of electron characteristic energy. (c) Electron temperature as function of partial electron density. The figure shows data from perijove 9 south. The best-fit parameters from orthogonal linear regressions in log-log space are given in the panels and in Table 2 for all the perijoves from this study.

is maximized. In a steady-state, field-aligned current, the current density scales with the magnetic field strength, which means that the drift velocity scales as B/n. Furthermore, the same scaling applies to the parallel electric field from inertial Alfvén waves, where the important parameter is the product of the perpendicular wave number, $k_\perp$, with the electron inertial length, λ_e, such that $E_\parallel \sim k_\perp^2 \lambda_e^2$ (Lysak & Song, 2000). The perpendicular wave number scales as the inverse of the distance between field lines, thus $k_\perp = B^{\frac{1}{2}}$. The electron inertial length scale is inversely proportional to the square root of electron density ($\lambda_e \sim n^{\frac{-1}{2}}$). Therefore, the parallel electric field again scales as B/n. A similar argument was used in Saur et al. (2018) where the energy of an Alfvén wave stays within a fluxtube whose width is inversely proportional to the square root of B.

Figure 9a shows the quantity B/n as a function of the magnetic latitude of Juno's footpoint for the perijove 9 south pass. The ratio increases with latitude and is largest close to ZI. Figure 9b shows a similar trend with the electron characteristic energy. It increases with latitude until ZI and keeps on increasing afterward (where JADE cannot determine the electron density). The characteristic energy, however, does not directly

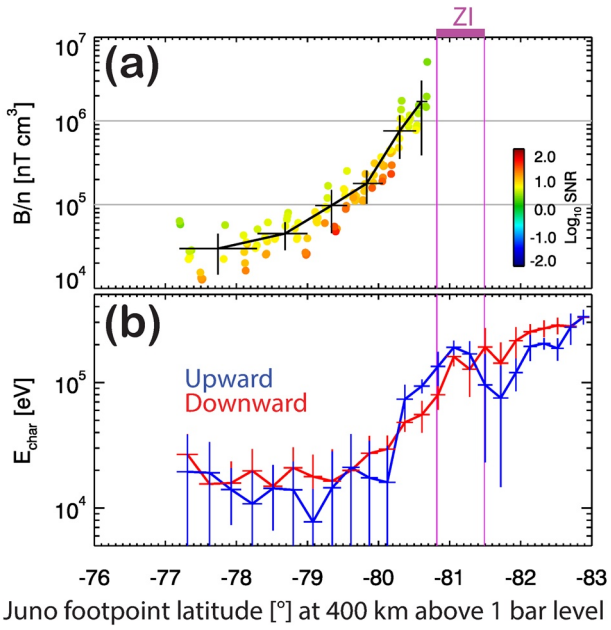

Figure 9. (a) Ratio B/n as a function of Juno footprint. (b) Characteristic energy of electrons within the loss cone. Blue is for upward-going (away from Jupiter) and red for downward-going (towards Jupiter) electrons. The ratio B/n increases with latitude and is largest near ZI. The characteristic energy of the electrons follows a similar trend. This is consistent with the formation of parallel electric fields capable of accelerating the electrons (see text for details).

reflect the local electric field $E_{||}$ at the position of Juno, but the integrated $E_{||}$ along a field line up to the position of Juno. B/n increases in Figure 9a by two orders of magnitude while the associated E_{char} only increases by approximately one order of magnitude. This difference might result from $E_{||}$ contributions to E_{char} along the crossed field lines not sampled during the flyby.

3. Summary and Conclusion

Our investigation presents electron densities and temperatures in the auroral region of Jupiter's main emissions. We use plasma data taken with the electron sensor of Jovian Auroral Distributions Experiment (JADE-E) and determine these quantities using numerical moments. Since JADE-E does not always measure the full electron distribution, we refer to partial densities. However, we keep the term electron temperature even though the derived electron temperature could also be affected for the same reason. This survey utilizes data from the first eight science perijoves for which JADE-E has better viewing conditions than subsequent perijoves. We use three criteria to select the JADE data: the signal-to-noise ratio is above 2, the full pitch angle distribution is measured, and the peak contribution to the density per energy channel is within JADE-E's energy range. After applying these criteria, we demonstrate that the electron density from JADE agrees within a factor of ~2 with the total electron density from Waves when the comparison is possible. Poleward of the main oval, the electron energies are usually in the upper part of JADE's energy range, and the densities tend to be very low (i.e., low signal). Equatorward of the diffuse aurora region, the background due to penetrating radiation is high and the electron energies fall below JADE-E's energy range.

Our main findings are:

1. The electron partial density increases from ~0.01 or 0.1 cm^{-3} near the main oval (or near Zone I as defined in Mauk et al., 2020) to a few cm^{-3} at the edge of the measurable part of the UV emission in the diffuse aurora region (DifA). The electron temperature is highest near the main oval at ~10–20 keV and decreases equatorward down to ~0.3–2 keV (Figures 2 and 5–7, and Table 2)
2. The JADE electron partial density agrees within a factor of ~2, with the total electron densities derived from Juno-Waves when it is possible to determine the density with both instruments (Figure 4)
3. The density and temperature trends (finding 1 above) are observed at all sampled longitudes, north and south. Similarly, these trends are independent of altitude in the range of the passes for this study (1.25–1.96 R_J). (Figures 6 and 7)
4. The electron density is anti-correlated with the temperature and the characteristic energy, and the temperature is correlated with the characteristic energy. We fit each pair with power laws (e.g., Figure 8) and provide the exponents in Table 2
5. In the region where JADE-E can determine the partial electron density, the ratio of B/n is maximum near Zone I. The characteristic energy of the electrons follows the same trend as the ratio B/n (Figure 9)

The combination of the JADE and Waves data sets provide additional information when compared to a single instrument data set. JADE and Waves can determine the electron densities in different regions, thereby extending the knowledge of this very important parameter in the auroral regions.

Data Availability Statement

The data presented here resides at NASA's Planetary Data System (https://pds-ppi.igpp.ucla.edu/mission/JUNO), and we used the following data sets: JNO-J_SW-JAD-3-CALIBRATED-V1.0, JNO-E/J/SS-WAV-3-CDR-BSTFULL-V1.0, and JNO-J-3-FGM-CAL-V1.0. The data from the figures is publicly available on a permanent repository at the following address: https://doi.org/10.5281/zenodo.5082196.

Acknowledgments
We thank all the outstanding women and men who have made Juno and its instrument suite so successful. The authors would also like to thank the following individuals who have helped in different capacities: George Hospodarsky, Masafumi Imai, Bob Lysak, and Craig Pollock. This work was funded by the NASA New Frontiers Program for Juno, at the University of Iowa through contract 699041X, at the University of Colorado through contract 699050X, and at Princeton University through contract NNM06AA75C with the Southwest Research Institute.

References

Allegrini, F., Gladstone, G. R., Hue, V., Clark, G., Szalay, J. R., Kurth, W. S., et al. (2020). First report of electron measurements during a Europa footprint tail crossing by Juno. *Geophysical Research Letters*, *47*, 1–10. https://doi.org/10.1029/2020GL089732

Allegrini, F., Mauk, B., Clark, G., Gladstone, G. R., Hue, V., Kurth, W. S., et al. (2020). Energy flux and characteristic energy of electrons over Jupiter's main auroral emission. *Journal of Geophysical Research: Space Physics*, *125*, e2019JA027693. https://doi.org/10.1029/2019JA027693

Bagenal, F., Adriani, A., Allegrini, F., Bolton, S. J., Bonfond, B., Bunce, E. J., et al. (2017). Magnetospheric science objectives of the Juno mission. *Space Science Reviews*, *213*, 219–287. https://doi.org/10.1007/s11214-014-0036-8

Bagenal, F., & Dols, V. (2020). The space environment of Io and Europa. *Journal of Geophysical Research: Space Physics*, *125*, e2019JA027485. https://doi.org/10.1029/2019JA027485

Bagenal, F., Wilson, R. J., Siler, S., Paterson, W. R., & Kurth, W. S. (2016). Survey of Galileo plasma observations in Jupiter's plasma sheet. *Journal of Geophysical Research: Planets*, *121*, 871–894. https://doi.org/10.1002/2016JE005009

Bame, S. J., Barraclough, B. L., Feldman, W. C., Gisler, G. R., Gosling, J. T., Mccomas, D. J., et al. (1992). Jupiter's magnetosphere: Plasma description from the Ulysses flyby. *Science*, *257*(5076), 1539–1543. https://doi.org/10.1126/science.257.5076.1539

Barnhart, B. L., Kurth, W. S., Groene, J. B., Faden, J. B., Santolik, O., & Gurnett, D. A. (2009). Electron densities in Jupiter's outer magnetosphere determined from Voyager 1 and 2 plasma wave spectra. *Journal of Geophysical Research*, *114*, A05218. https://doi.org/10.1029/2009JA014069

Bolton, S. J., Lunine, J., Stevenson, D., Connerney, J. E. P., Levin, S., Owen, T. C., et al. (2017). The Juno mission. *Space Science Reviews*, *213*, 5–37. https://doi.org/10.1007/s11214-017-0429-6

Bonfond, B., Gladstone, G. R., Grodent, D., Greathouse, T. K., Versteeg, M. H., Hue, V., et al. (2017). Morphology of the UV aurorae Jupiter during Juno's first perijove observations. *Geophysical Research Letters*, *44*(10), 4463–4471. https://doi.org/10.1002/2017GL073114

Clark, G., Mauk, B. H., Haggerty, D., Paranicas, C., Kollmann, P., Rymer, A., et al. (2017). Energetic particle signatures of magnetic field-aligned potentials over Jupiter's polar regions. *Geophysical Research Letters*, *44*(17), 8703–8711. https://doi.org/10.1002/2017GL074366

Clark, G., Tao, C., Mauk, B. H., Nichols, J., Saur, J., Bunce, E. J. J., et al. (2018). Precipitating electron energy flux and characteristic energies in Jupiter's main auroral region as measured by Juno/JEDI. *Journal of Geophysical Research: Space Physics*, *123*(9), 7554–7567. https://doi.org/10.1029/2018JA025639

Clarke, J., Grodent, D., Cowley, S., Bunce, E., Zarka, P., Connerney, J., & Satoh, T. (2004). Jupiter's aurora. In F. B. Magnetosphere, T. E. Dowling, & W. B. McKinnon (Eds.), *Jupiter: Planet, satellites*. Cambridge University Press.

Clarke, J. T., Ballester, G. E., Trauger, J., Ajello, J. M., Pryor, W. R., Tobiska, K., et al. (1998). Hubble Space Telescope imaging of Jupiter's UV aurora during the Galileo orbiter mission of Jupiter's aurora have been obtained close in time with Galileo ultraviolet spectrometer (UVS) spectra and in situ particles, fields, and plasma of the equa. *Journal of Geophysical Research*, *103*(98), 20. https://doi.org/10.1029/98je01130

Connerney, J. E. P., Acuña, M. H., & Ness, N. F. (1981). Jovian current sheet and inner magnetosphere. *Journal of Geophysical Research*, *86*(A10), 8370–8384. https://doi.org/10.1029/JA086iA10p08370

Connerney, J. E. P., Acuna, M. H., Ness, N. F., & Satoh, T. (1998). New models of Jupiter's magnetic field constrained by the Io flux tube footprint. *Journal of Geophysical Research*, *103*, 11929–11939. https://doi.org/10.1029/97JA03726

Connerney, J. E. P., Benn, M., Bjarno, J. B., Denver, T., Espley, J., Jorgensen, J. L., et al. (2017). The Juno magnetic field investigation. *Space Science Reviews*, *213*, 39–138. https://doi.org/10.1007/s11214-017-0334-z

Connerney, J. E. P., Kotsiaros, S., Oliversen, R. J., Espley, J. R., Joergensen, J. L., Joergensen, P. S., et al. (2018). A new model of Jupiter's magnetic field from Juno's first nine orbits. *Geophysical Research Letters*, *45*, 2590–2596. https://doi.org/10.1002/2018GL077312

Cowley, S. W. H., & Bunce, E. J. (2001). Origin of the main auroral oval in Jupiter's coupled magnetosphere-ionosphere system. *Planetary and Space Science*, *49*(10–11), 1067–1088. https://doi.org/10.1016/S0032-0633(00)00167-7

Damiano, P. A., Delamere, P. A., Stauffer, B., Ng, C. S., & Johnson, J. R. (2019). Kinetic simulations of electron acceleration by dispersive scale Alfvén Waves in Jupiter's magnetosphere. *Geophysical Research Letters*, *46*(6), 3043–3051. https://doi.org/10.1029/2018GL081219

Elliott, S. S., Sulaiman, A. H., Kurth, W. S., Faden, J., Allegrini, F., Valek, P., et al. (2021). The high-latitude extension of Jupiter's Io torus: Electron densities measured by Juno Waves. *Journal of Geophysical Research: Space Physics*, *126*, e2021JA029195. https://doi.org/10.1029/2021JA029195

Gladstone, G. R., Persyn, S. C., Eterno, J. S., Walther, B. C., Slater, D. C., Davis, M. W., et al. (2017). The ultraviolet spectrograph on NASA's Juno mission. *Space Science Reviews*, *213*, 447–473. https://doi.org/10.1007/s11214-014-0040-z

Hill, T. W. (1979). Inertial limit on corotation. *Journal of Geophysical Research*, *84*(9), 6554–6558. https://doi.org/10.1029/JA084iA11p06554

Hill, T. W. (2001). The Jovian auroral oval. *Journal of Geophysical Research*, *106*(A5), 8101–8107. https://doi.org/10.1029/2000JA000302

Khurana, K., Kivelson, M. G., Vasyliunas, V., Krupp, N., Woch, J., Lagg, A., et al. (2004). The configuration of Jupiter's magnetosphere. In D. Bagenal, & McKinnon (Eds.), *Jupiter: Planet, satellites, magnetosphere*. Cambridge University Press.

Knight, S. (1973). Parallel electric fields. *Planetary and Space Science*, *21*, 741–750. https://doi.org/10.1016/0032-0633(73)90093-7

Kotsiaros, S., Connerney, J. E. P., Clark, G., Allegrini, F., Gladstone, G. R., Kurth, W. S., et al. (2019). Birkeland currents in Jupiter's magnetosphere observed by the polar-orbiting Juno spacecraft. *Nature Astronomy*, *3*, 904–909. https://doi.org/10.1038/s41550-019-0819-7

Krupp, N., Vasyliunas, V., Woch, J., Lagg, A., Khurana, K., Kivelson, M., et al. (2004). Dynamics of the Jovian magnetosphere. In F. Bagenal, T. E. Dowling, & W. B. McKinnon (Eds.), *Jupiter: Planet, satellites, magnetosphere*. Cambridge University Press.

Kurth, W. S., Hospodarsky, G. B., Kirchner, D. L., Mokryzcki, B. T., Averkamp, T. F., Robison, W. T., et al. (2017). The Juno waves investigation. *Space Science Reviews*, *213*(1), 347–392. https://doi.org/10.1007/s11214-017-0396-y

Lysak, R. L., & Hudson, M. K. (1979). Coherent anomalous resistivity in the region of electrostatic shocks. *Geophysical Research Letters*, *6*(8), 661–663. https://doi.org/10.1029/GL006i008p00661

Lysak, R. L., & Song, Y. (2000). The role of Alfvén waves in the formation of auroral parallel electric fields (pp. 147–155). https://doi.org/10.1029/GM118p0147

Mauk, B. H., Clark, G., Gladstone, G. R., Kotsiaros, S., Adriani, A., Allegrini, F., et al. (2020). Energetic particles and acceleration regions over Jupiter's polar cap and main aurora: A broad overview. *Journal of Geophysical Research: Space Physics*, *125*(3), 1–25. https://doi.org/10.1029/2019JA027699

Mauk, B. H., Haggerty, D. K., Jaskulek, S. E., Schlemm, C. E., Brown, L. E., Cooper, S. A., et al. (2017). The Jupiter energetic particle detector instrument (JEDI) investigation for the Juno mission. *Space Science Reviews*, *213*(1–4), 289–346. https://doi.org/10.1007/s11214-013-0025-3

Mauk, B. H., Haggerty, D. K. K., Paranicas, C., Clark, G., Kollmann, P., Rymer, A. M. M., et al. (2018). Diverse electron and ion acceleration characteristics observed over Jupiter's main aurora. *Geophysical Research Letters*, *45*(3), 1277–1285. https://doi.org/10.1002/2017GL076901

Mauk, B. H., Haggerty, D. K., Paranicas, C., Clark, G., Kollmann, P., Rymer, A. M., et al. (2017). Juno observations of energetic charged particles over Jupiter's polar regions: Analysis of monodirectional and bidirectional electron beams. *Geophysical Research Letters*, *44*(10), 4410–4418. https://doi.org/10.1002/2016GL072286

Mauk, B. H., Mitchell, D. G., McEntire, R. W., Paranicas, C. P., Roelof, E. C., Williams, D. J., et al. (2004). Energetic ion characteristics and neutral gas interactions in Jupiter's magnetosphere. *Journal of Geophysical Research*, *109*, A09S12. https://doi.org/10.1029/2003JA010270

McComas, D. J., Alexander, N., Allegrini, F., Bagenal, F., Beebe, C., Clark, G., et al. (2017). The Jovian auroral distributions experiment (JADE) on the Juno mission to Jupiter. *Space Science Reviews*, *213*(1–4), 547–643. https://doi.org/10.1007/s11214-013-9990-9

McComas, D. J., Allegrini, F., Bagenal, F., Crary, F., Ebert, R. W., Elliott, H., et al. (2007). Diverse plasma populations and structures in Jupiter's magnetotail. *Science*, *318*, 217–220. https://doi.org/10.1126/science.1147393

McComas, D. J., & Bagenal, F. (2007). Jupiter: A fundamentally different magnetospheric interaction with the solar wind. *Geophysical Research Letters*, *34*, 20. https://doi.org/10.1029/2007GL031078

McIlwain, C. E. (1961). Coordinates for mapping the distribution of magnetically trapped particles. *Journal of Geophysical Research*, *66*, 3681–3691. https://doi.org/10.1029/JZ066i011p03681

Paschmann, G., & Daly, P. W. (1998). Analysis Methods for Multi-Spacecraft Data. ISSI Scientific Reports Series SR-001, Vol. 1. ISBN 1608-280X.

Saur, J., Janser, S., Schreiner, A., Clark, G., Mauk, B. H., Kollmann, P., et al. (2018). Wave-particle interaction of Alfvén waves in Jupiter's magnetosphere: Auroral and magnetospheric particle acceleration. *Journal of Geophysical Research: Space Physics*, *123*, 9560–9573. https://doi.org/10.1029/2018JA025948

Saur, J., Pouquet, A., & Matthaeus, W. H. (2003). An acceleration mechanism for the generation of the main auroral oval on Jupiter. *Geophysical Research Letters*, *30*, 1260. https://doi.org/10.1029/2002GL015761

Scudder, J. D., Sittler, E. C., & Bridge, H. S. (1981). A survey of the plasma electron environment of Jupiter: A view from Voyager. *Journal of Geophysical Research*, *86*(A10), 8157–8179. https://doi.org/10.1029/ja086ia10p08157

Sittler, E. C., & Strobel, D. F. (1987). Io plasma torus electrons: Voyager 1. *Journal of Geophysical Research*, *92*(A6), 5741. https://doi.org/10.1029/ja092ia06p05741

Szalay, J. R., Allegrini, F., Bagenal, F., Bolton, S. J., Bonfond, B., Clark, G., et al. (2020). Alfvénic acceleration sustains Ganymede's footprint tail aurora. *Geophysical Research Letters*, *47*(3), 1–10. https://doi.org/10.1029/2019GL086527

Szalay, J. R., Bonfond, B., Allegrini, F., Bagenal, F., Bolton, S., Clark, G., et al. (2018). In situ observations connected to the Io footprint tail aurora. *Journal of Geophysical Research: Planets*, *123*, 3061–3077. https://doi.org/10.1029/2018JE005752

Thomas, N., Bagenal, F., Hill, T., & Wilson, J. (2004). The Io neutral clouds and plasma torus. In *Jupiter: Planet, satellites, magnetosphere*, In F. Bagenal, T. E. Dowling, and W. B. McKinnon (Eds.), Cambridge University Press.